Fall 12-2013

STRUCTURAL & MAGNETIC CHARACTERIZATION STUDY OF $HfCo_7$ ALLOY WITH SUBSTITUTIONS OF Si, Ti, Fe, Mn & B

Jacob A. Lewis
University of Nebraska-Lincoln, jacob.alan.lewis@gmail.com

STRUCTURAL & MAGNETIC CHARACTERIZATION STUDY OF $HfCo_7$ ALLOY WITH SUBSTITUTIONS OF Si, Ti, Fe, Mn &B

by

Jacob A. Lewis

A THESIS

Presented to the Faculty of

The Graduate College at the University of Nebraska

In Partial Fulfillment of Requirements

For the Degree of Master of Science

Major: Mechanical Engineering & Applied Mechanics

Under the Supervision of Professor Jeffrey E. Shield

Lincoln, Nebraska

December, 2013

STRUCTURAL & MAGNETIC CHARACTERIZATION STUDY OF $HfCo_7$ ALLOY WITH SUBSTITUTIONS OF Si, Ti, Fe, Mn &B

Jacob Alan Lewis, M.S.

University of Nebraska, 2013

Adviser: Jeffrey E. Shield

Magnetic materials are a critical component of the modern technological society. The market of high-energy product hard magnets is dominated by the rare-earth element containing neodymium-iron-boron (NdFeB) magnets. As a result of worldwide demand coupled with trade restrictions on rare-earth minerals, new magnet compositions are explored to reduce pressure on the already strained market. The hafnium-cobalt alloy system has shown promise as a candidate for filling the gap in saturation magnetization between rare-earth containing alloys and those made with abundant elements. This study explores the magnetic effects of silicon, titanium, iron, manganese and boron substitutions in the hafnium-cobalt-7 (1:7 atomic ratio) alloy.

The compositions investigated followed the $HfCo_{7-x}(Si, Ti, Fe, Mn, B)_x$ (x = 0, 0.5, 1 for Si, Fe, Mn, B | x=0, 0.25, 0.5 for Ti) atomic formula. All specimens were produced by arc melting followed by melt spinning (crucible orifice diameter of 0.5mm and wheel speed of 10 m/s). Structural information was obtained with an x-ray diffractometer (XRD) and atom probe tomography (APT). Magnetic measurements were performed in a super-conducting quantum interference device (SQUID).

The silicon and titanium substitutions caused the disappearance of the orthorhombic phase and a large reduction in magnetization. Substitution of cobalt for iron atoms did not affect the coercivity but increases magnetic susceptibility. In the case of the manganese, the original phase was not present. There is an increase of about 7.5% magnetization at 50 kOe for the $HfCo_6Mn$ composition (101 emu/g at 50 kOe) and higher magnetic susceptibility. However, these alloys have very little coercivity. The boron samples were found to retain the structure of the base alloy with additional regions of a boron-rich phase. This second phase is responsible for separation of magnetic domains, increasing coercivity from 0.42 kOe to 4.49 kOe for $HfCo_6B_{0.75}$ (an increase of nearly 10x). However, the non-magnetic phase reduces the magnetization at 50 kOe of the bulk material by approximately 30%.

Table of Contents

List of Figures

Author's Acknowledgements

I would like to first thank my adviser, Dr. Jeffrey Shield, for his continued guidance throughout my graduate experience. Without his support, none of the following would be possible.

I would also like to express my gratitude to my mentor in France, Dr. Jean-Marie Le Breton, for his essential supervision and hospitality in France. I would like to express my gratitude to Dr. Mehrdad Negahban and Dr. Jean-Marc Saiter, for their assistance and leadership in EMME program; and Dr. Antonella Esposito, for her help and kindness throughout my time abroad.

Furthermore, to my colleagues at UNL and UR for your continuous advice and friendship, I thank you. Especially, I would also like to thank Emeric Folcke for his help and advice both in and out of the lab.

Finally, I would like to acknowledge the encouragement and support of all my friends and my family. Thank you to all my friends, near and far, for being apart of my journey. To all my family, I love you.

And most importantly, I would like to thank my parents for their endless love and support throughout my life. Thank you for everything mom and dad, I love you.

Grant Information

The research presented in this study was funded through the U.S. Department of Energy – Advanced Research Projects Agency – Energy (arpa-E). The mobility funding for travel and study at the Université de Rouen, France, was provided through the U.S. Department of Education Fund for Improvement of Post-Secondary Education (FIPSE-ATLANTIS) and the European Union Erasmus Mundus programs.

Chapter 1:
INTRODUCTION

Magnetic materials have been of interest to humans for thousands of years. Magnetite (Fe_3O_4) was observed to display its strange properties as early as the first half of the second millennium BC in Mesopotamia.[1] Eventually mankind made use of the magnetic phenomenon in the form of the compass, which aligned with the natural magnetic field of Earth. Over the last century, magnets have become an indispensible component of modern technology, with extensive applications ranging from data storage to power generation (e.g. wind turbines) and utilization (e.g. electric vehicle motors).

1.1 Motivation

The recent push toward renewable energy and green technology has created a surge in the demand for magnets. However, the highest energy product magnets require rare-earth elements such as samarium (Sm) and neodymium (Nd). Additionally, there is a large gap in maximum energy product between alloys that contain rare-earth elements and those that do not. This gap is illustrated in Figure 1, with a difference of about 10 MGOe between Alnico and the samarium containing alloys. The increasing worldwide demand for rare-earth magnets has caused a dramatic increase in prices. Furthermore, the supply of rare-earth minerals is strongly limited by both political and environmental sanctions. The mining and refining of these elements has environmentally hazardous waste, which had been cost-prohibitive for execution in the United States due to burdensome regulations compared to the relaxed policies of other countries. Consequently, these rare-earth elements have been determined to be critically strategic to the future of American

technology and energy requirements. Dysprosium (Dy) was considered the most critical rare-earth resource in the near to medium range future according the U.S. Department of Energy.[2] Dysprosium is used in Nd-Fe-B magnets to augment coercivity and to guard against demagnetization at high temperatures. As a result, magnets for high temperature applications place a higher strain on the rare-earth market.

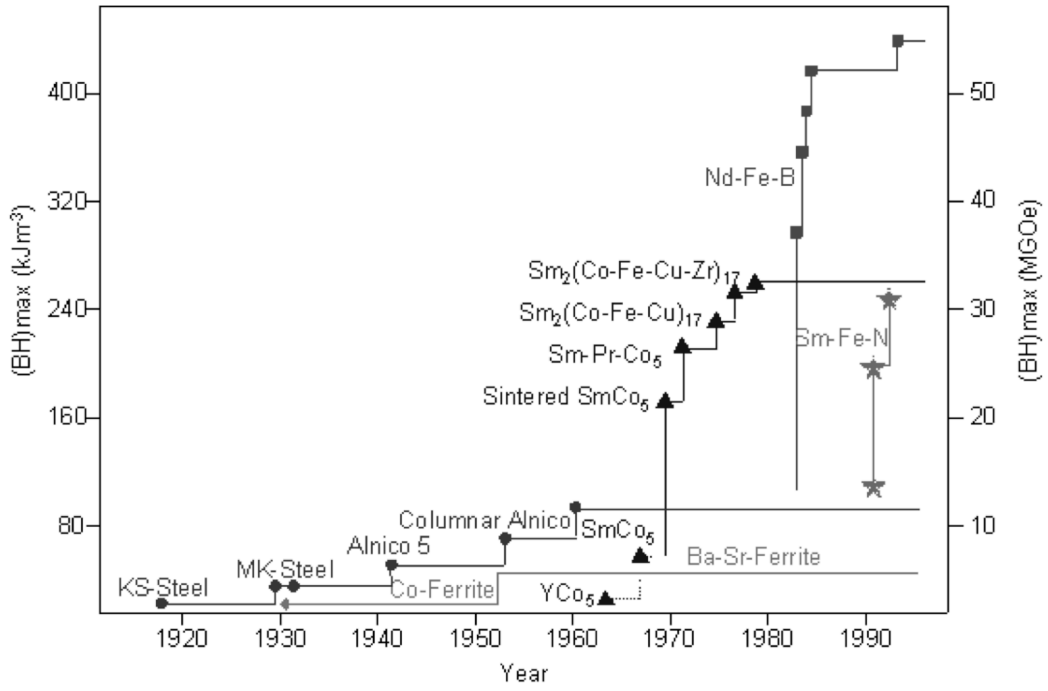

Figure 1 - Development of magnets maximum energy product through the years.[3]

The output supply of rare-earth minerals is dominated by China, with over 95% of production in the world.[4] Due to the strategic nature of these minerals and China's own modernization, the strained market is subjected to further tariffs and trade restrictions that exacerbate the situation. Therefore, non-rare-earth magnets are sought after to replace current high-energy and/or high temperature magnets with cheaper and/or indigenous materials. Additionally, any magnetic materials that can bridge the energy product gap could reduce the strain on the rare-earth market.

Consequently, there is a healthy drive in research to develop non-rare-earth magnets, for example the alloy systems of MnAl, MnBi, and Zr_2Co_{11}. These materials are studied for the same objectives as this hafnium-cobalt investigation. MnAl with C is reported as having a coercivity as high as 4.6 kOe following proper processing techniques.[5] The saturation magnetization is reported as decreasing with increasing coercivity as a result of equilibrium phase formation. A similar system makes use of the addition of FeCo nanoparticles to induce exchange coupling. The nanoparticle of FeCo were reported as having saturation of 175 emu/g and a coercivity of 112 Oe.[6] However, the use of nanoparticles limits the ability to upscale these materials into widespread implementation. Therefore, other production methods such as melt spinning, which can be up scaled easily, are more lucrative for implementation in the international marketplace. The MnBi alloy system is also being examined by researchers because of the phenomenon of having an increasing coercivity with increasing temperature. This material, in aligned powder form, is reported as having a coercivity of 13.6 kOe at room temperature.[7] Another material of interest to magnetic research is Zr_2Co_{11} compound. It has been described as reaching coercivity as high as 2.9 kOe.[8] Hafnium-cobalt is similar to the Zr_2Co_{11} compound in structure, both being orthorhombic.[9] Additionally, the chemical similarity between hafnium and zirconium potentially could have the same effects in an alloy. $HfCo_7$ has a relatively high Curie temperature (600 K)[10] and, at least in this investigation, is produced using scalable techniques for potential mass production. Therefore, the hafnium-cobalt alloy and its potential modification is a worthwhile study in the realm of permanent magnetics.

1.2 Magnetism

The source of magnetism in a material is a result of unpaired inner shell electrons surrounding the individual atoms. The fundamental relationship between magnetism and electricity, specifically circulating currents, was originally proposed by Oersted in 1820.[11] Oersted proposed that some magnetic moment (m) is equal to a circulating current (I) times the area of the loop (A) as shown in the following equation:

$$m = IA$$

The orbiting electrons around a nucleus act in the same way as a current flowing through a wire, merely on a different order of size. Each orbiting electron is a circulating electrical current that creates a small magnetic moment. When electrons are paired in their orbitals, the moments cancel each other out. However, in the case of an unpaired electron orbiting the enormous number of nuclei in a material results in the phenomenon of magnetism.

Magnetic materials can be categorized into several groups based on the behavior of their spin configurations. The major orderings are ferromagnetic, antiferromagnetic, ferrimagnetic and paramagnetic. The classification is based on the orientation of magnetic moments within the material. Ferromagnetic materials have magnetic moments of the constituent atoms aligned in the same direction. Antiferromagnetic materials have antiparallel aligned moments where the net magnetization is zero, while ferrimagnetic materials have the same arrangement but with a non-zero net magnetization. The non-zero net magnetization in ferrimagnetic materials result from two different magnitudes of moments that are coupled anti-parallel. Paramagnetic materials have zero net magnetization due to randomness of internal magnetic moments. Ferromagnetic

materials become paramagnetic above its Curie temperature, as the thermal energy overpowers the ordering of the moments.

The magnetic properties of ferromagnetic and ferrimagnetic materials are generally determined by measurement of magnetization versus applied external field. This relationship is represented as a hysteresis loop. A typical hysteresis loop for a ferromagnetic material is shown in Figure 2. A magnetometer (such as a super-conducting quantum interference device, or SQUID, that was used in this study) typically performs a full loop by applying a magnetic field (H) from zero up to a maximum (H_{max}), from point O to A in Figure 2. The field is then progressively changed to the maximum applied field with the field going in the opposite direction ($-H_{max}$), which is shown at B in the figure (at this point it is considered a half loop). The field returns to H_{max} (point A) to complete a full loop. The device records the magnetization of the tested material at prescribed intervals and conditions. There are three important extrinsic properties that can be determined directly from the hysteresis loop. The saturation magnetization (M_s) is the highest value of magnetization a material exhibits, generally determined as the limit of the flattening curve in higher applied fields. Remnant magnetization (M_r) is the strength of magnetization of the material when the applied field is zero. Coercivity (H_c) is the field that demagnetizes the material, or the field that causes the magnetization to return to zero.

A material can be classified as a hard (permanent) or soft magnet based on the level of its coercivity. Magnetically hard materials can be considered to be those with coercivity greater than 2.5 kOe (200 kA/m), while a soft material is less than 12.6 Oe (1 kA/m).[11] The materials with coercivity values between 12.6 Oe (1 kA/m) and 2.5 kOe (200 kA/m)

deemed semi-hard magnets. These materials are used in magnetic recording devices, such as computer hard disk drives

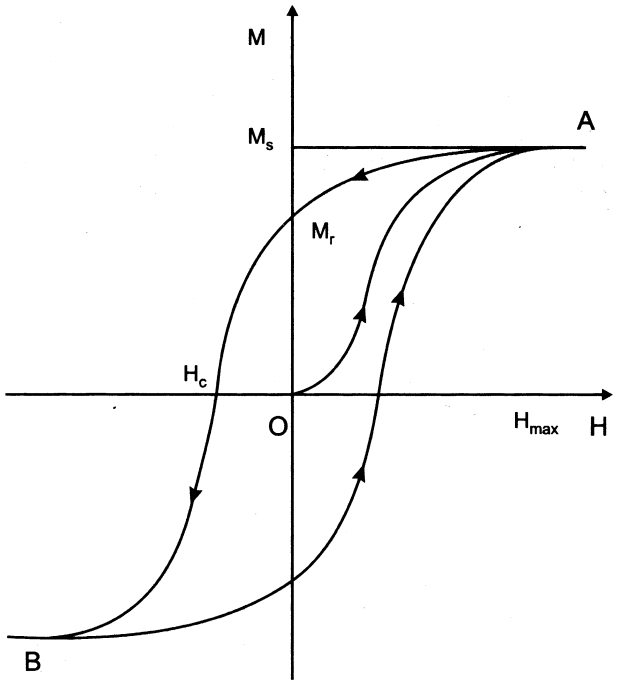

Figure 2 - General magnetic hysteresis loop for a ferromagnetic material.[1]

Size, shape and orientation of a sample can have an effect on the observed magnetization. The internal field (H') of a finite piece of material is composed of the applied field (H) and a demagnetizing field (H_{dm}), $H' = H + H_{dm}$.[11] The demagnetizing field can be represented as a constant (D) that is proportional to the magnetization (M) of the material, $H_{dm} = -DM$. The demagnetizing factor is unique for each major axis for a given geometry (D_x, D_y, D_z) and these should sum to one. Thus, orientation during any experiment should be considered to reduce influence of the demagnetizing field from sample geometry.

1.3 Literature Review

$HfCo_7$ is an intermetallic compound that is the primary focus of this study. It is a cobalt-based compound with 12.5 at% Hf that appears as stable between 1050 ºC to 1250 ºC in the phase diagram (Figure 3). Buschow first reviewed it for its magnetic properties. It was reported as having a hexagonal structure (a = 5.477 Å, c = 8.070 Å) with Curie temperature of 600K.[10] The structure, however, was reexamined using transmission electron microscope and was reported as having an orthorhombic structure, space group *Pcna* (a = 4.7 Å, b = 8.3 Å, c = 38 Å).[9] Additionally, Demczyk and Cheng suggest that the compound unit cell is comprised of two long-period superlattices in antiphase relation along [001].

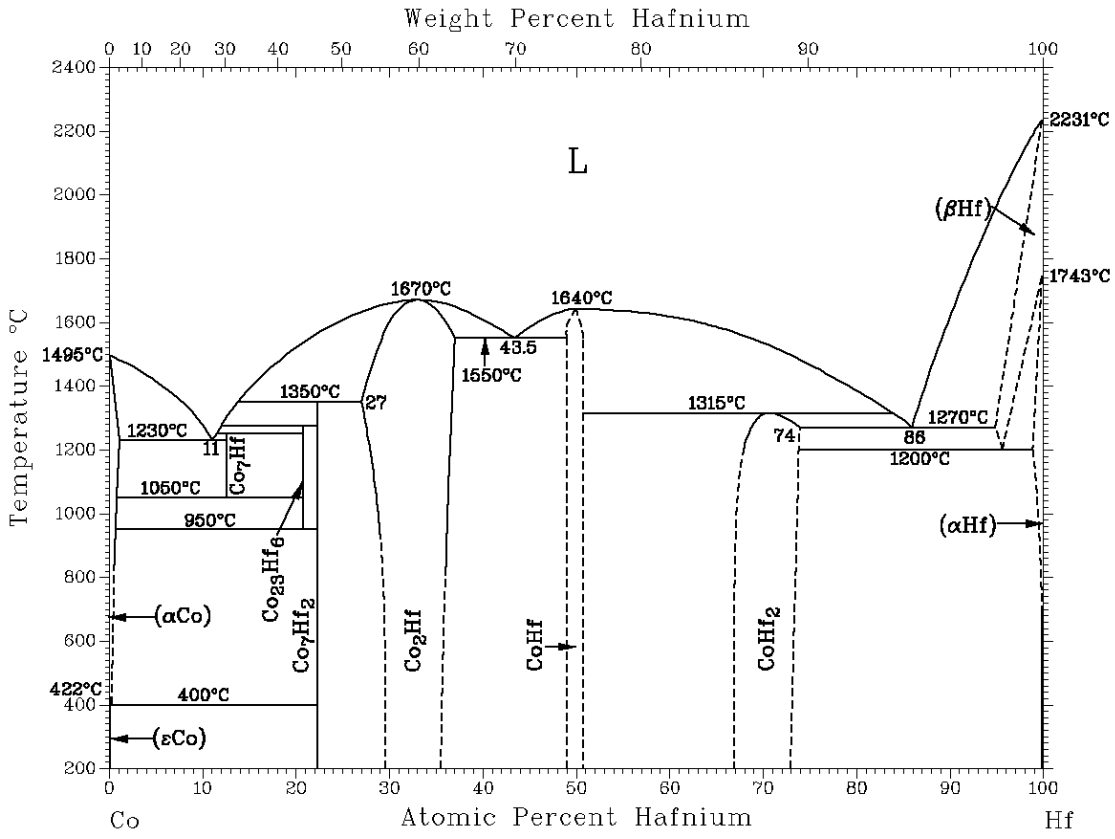

Figure 3 - Hafnium and cobalt binary system phase diagram.[12]

Recently, the $HfCo_7$ has become of interest to researchers due to its high Curie temperature and potential as a permanent magnet candidate. The latest investigations agree with the orthorhombic structure but reporting the lattice parameters as: a = 4.7189 Å, b = 4.2783 Å, and c = 8.0705 Å.[13] Balamurugan, et al. explored $HfCo_7$ nanoparticles in particular, but also examined the material as a melt spun bulk form, which was reported as not yet attaining magnetic saturation in an applied field (H) of 70 kOe (7 T) as a result of high magnetic anisotropy. The magnetic properties for these melt-spun bulk materials were reported as H_c = 1.8 kOe (0.18 T) and M = 725 emu/cm^3 (for H=50 kOe and T = 300 K).[13] The effects of substitutions and additions in the $HfCo_7$ alloy have not been previously reported in literature and thus compel exploration to determine the influence on magnetic and structural properties.

Chapter 2:
EXPERIMENTAL DETAILS

2.1 Materials

High-purity cobalt (Co), hafnium (Hf), silicon (Si), titanium (Ti), iron (Fe), manganese (Mn) and boron (B) obtained from Alfa Aesar were used in the sample production. The purities were reported as 99.9+%, 99.9%, 99.99%, 99.5%, 99.99%, 99.99%, and 99.5% for Co, Hf, Si, Ti, Fe, Mn and B respectively. Hafnium is stated to have at most 2% zirconium (Zr) within the metal basis of the material. This is a result of the difficulty of separating Hf from Zr in its natural source. Additionally, the manganese pieces have a tendency to oxidize in atmosphere, and required sanding prior to use.

2.2 Sample Production

2.2.1 Arc Melting

Arc Melting is a technique used for alloy production that allows for high-degree of control in composition and homogeneity. High-purity materials are carefully weighed out according to the desired sample composition using a standard laboratory balance. The arc melting process was accomplished with the use of a custom laboratory device, designed specifically for ingot production. The elemental materials are placed in the arc melting apparatus' base, which is made of solid copper and cooled by flowing water during the process. The apparatus is assembled with its body and top pieces, and then placed under vacuum. In order to prevent the unwanted oxidation of the alloy, the chamber is backfilled with argon gas and is place under vacuum again. The process is repeated several times to ensure the level of oxygen is relatively insignificant. The

copper base is grounded while the top piece contains an arm with a tungsten electrode that can be manipulated from the outside. The electrode sheath is also made of copper and is cooled with flowing water to prevent damage to the apparatus. The power to the electrode in the laboratory-built apparatus used is supplied to the electrode by a Miller Syncrowave 180SD welding power supply. Initially, a small piece of zirconium, in a separate basin in the base-plate to prevent contamination, is melted and allowed to cool several times. The zirconium easily oxidizes in the presence of oxygen, and verifies the success of the vacuum-backfill process if the piece retains its initial luster. The elemental materials are then carefully melted together with the electrical arc, taking care to avoid splattering of the measured amounts. The elemental boron is particularly prone to splattering during the initial melting process, and therefore, requires particular care in stacking the elemental pieces and the first stages of melting all pieces together. The initial ingot is allowed to cool for several minutes before being carefully flipped with the electrode tip and re-melted. The flipping process is repeated to ensure optimal homogeneity. The final ingot and any splattered piece are collected and weighed to observe any loss of the materials and thus verify the target composition is effectively obtained. A diagram that shows the general configuration of the arc-melting device, along with a photograph of the process occurring, can be seen in Figure 4.

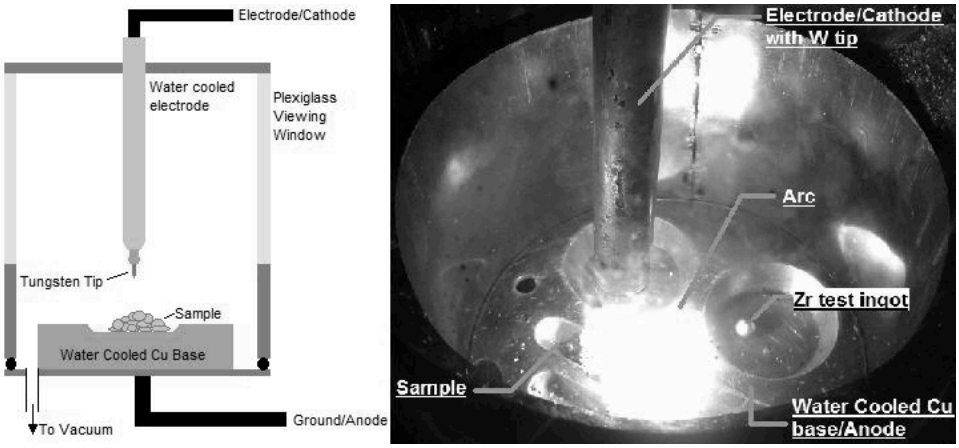

Figure 4 – Arc melting device diagram (lt) and a photo of arc melting in progress (rt).[14]

2.2.2 Melt Spinning

Melt spinning is a process used for ultra-rapid solidification of metallic alloys. The process has the ability of cooling the material at a rate of upwards of 10^6 °C/s, which can lead to a variety of structures including amorphous, nanocrystalline and metastable structures. Metastable phases cannot be obtained through usual atmospheric cooling or quenching processes. The ingot formed during the arc melting process is placed in a quartz crucible, which has an orifice in the nozzle end. For the purposes of this investigation, a 0.5mm hole was used in all sample preparations. The crucible is mounted in the device with the sample being placed in the center of a water-cooled copper induction coil. The induction coil is used to fully melt the sample material just before "shooting". The melted sample is ejected out of the crucible hole by an over pressured tank of argon gas. The over-pressure is set at approximately 0.2 bar higher than the apparatus' ambient argon atmosphere. The crucible is directly above a spinning copper wheel, which the sample hits after leaving the crucible. The tip of the crucible is set perpendicular and approximately 5mm above the copper wheel. The stream of molten sample is solidified after contacting the spinning wheel, and is thrown off by centrifugal

force into the collection chamber of the melt spinner. The experimental setup and process is illustrated in Figure 5.

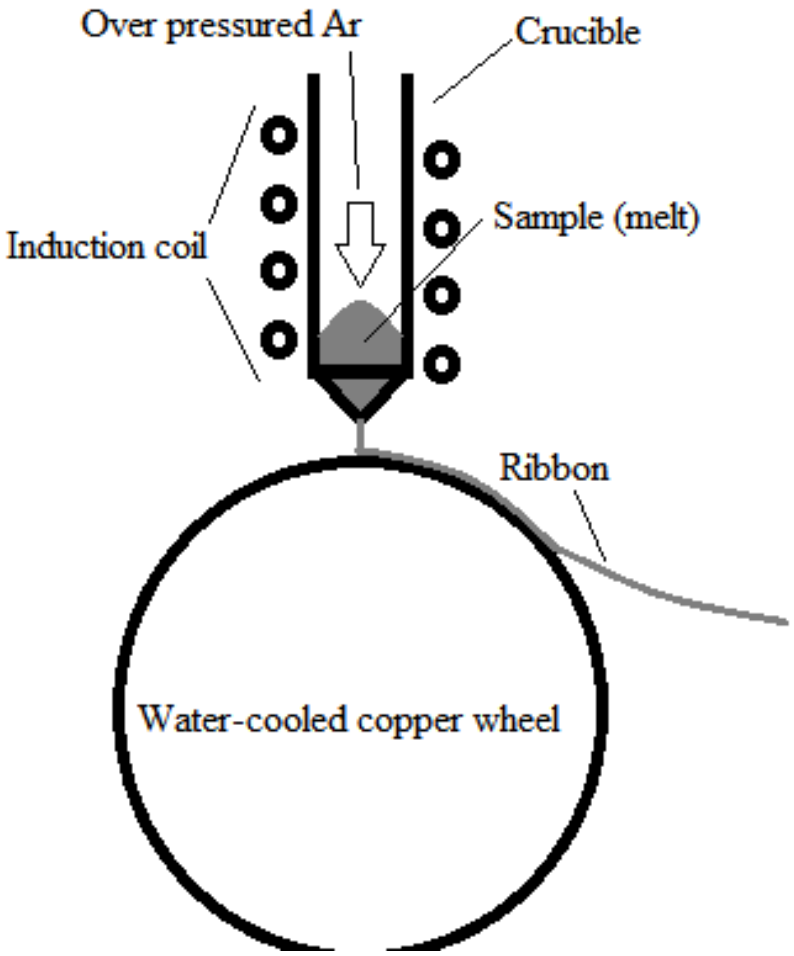

Figure 5 – Diagram of the melt spinning process.

The as-spun ribbons can then be collected for characterization and further processing as needed. A typical example of the ribbons produced by this method is shown in Figure 6. The sample shown in the figure shows the result of melt-spinning an approximately 5g ingot of a certain composition.

Figure 6 - Typical melt spun ribbons in storage container.

The samples studied were melt spun at 10m/s in order to limit experimental variables to only the effects of the sample composition. A SC Edmund-Buhler Gmbh melt spinner was used in the production of all samples in this investigation, which is shown in Figure 7.

Figure 7 - Edmund Bühler GmbH Melt Spinner SC

2.3 Characterization

2.3.1 X-ray Diffraction

The technique of x-ray diffraction is a cornerstone of crystallographic characterization in modern materials science. X-ray diffraction (XRD) relies on the interference of incident electromagnetic radiation after interacting with the regular spacing of atomic planes. As a result of the similar magnitudes of the wavelength of the incident beam and the atomic spacing, the waves cause constructive or destructive interference that produces a unique pattern of peaks that can be used to identify the crystal structure. The mathematical condition required for constructive diffraction to occur is represented by Bragg's Law:

$$n\lambda = 2d_{hkl}sin\theta$$

where n is any integer, λ is the x-ray wavelength, d_{hkl} is the interplanar spacing and θ is the angle of incidence. The samples were analyzed in their as-spun state using a single ribbon attached with tape to a zero-background silicon holder on both the wheel-side (side of ribbon contacting the copper wheel during melt spinning) and the free-side (side of ribbon open to ambient atmosphere in the melt spinning apparatus). The tape used to hold the ribbons flat is placed in such a way as to reduce its exposure to the incident x-ray beam. Additionally, tests analyzing only tape were performed to determine the effects of any exposed tape during sample analysis. A Bruker D8 Advanced Diffractometer at the GPM laboratory (Groupe de Physique des Matériaux in Rouen, France) with a cobalt source (35 kV, 40mA, 1.78897 Å) was used for all samples.

2.3.3 Magnetic Measurements

Magnetic measurements involve obtaining a hysteresis loop over a given range of applied magnetic field. A superconducting quantum interference device (SQUID) was used to obtain all magnetic measurements for this investigation. A SQUID is capable of testing small pieces of material under high magnetic fields over a range of temperatures with a high level of accuracy. The SQUID used for testing all reported materials is a Quantum Design Magnetic Property Measurement System (MPMS) that has a sample temperature range from 5K to 400K and a magnetic field range of -50 kOe (-5T) to 50 kOe (5T). Both temperature and field can be independently changed, allowing different experiments to be performed. The types of tests performed for this study involve full hysteresis loops from -50 kOe to 5 kOe at both 5K and 300K. Additionally, temperature sweeps from 5K to 400K with a constant applied field were performed on certain samples. The physical phenomena of flux quantization and Josephson tunneling are used in a SQUID to measure the response of a material in high fields.[15] Superconducting coils are cooled using liquid helium and are located very close to an installed sample. These coils detect the magnetic response of the specimen as temperature and applied field are changed. Modern SQUIDs are the most sensitive detectors of magnetic flux, with a resolution as small as a small fraction of a single flux quantum ($\sim 10^{-6}\ \Phi_0\ Hz^{-1/2}$).[16] The Quantum Design MPMS is reported to have a sensitivity of 1×10^{-8} emu @ 2,500 Oe.[17]

2.3.4 Atom Probe Tomography

Atom probe tomography (APT) is an advanced material characterization technique that analyzes the identity and position of atoms for a given sample. The resulting data allows post-processing software to reconstruct the millions of atoms into a visual representation

of atomic structure and composition changes within the sampled piece. The three dimensional tomographic atom probe (TAP) technique was developed in the 1980s by M.K. Miller, based on the preceding technology of imaging atom probe (IAP).[18] The process requires a lengthy and delicate sample preparation and is a destructive technique such that the examined portion the material is non-recoverable following analysis.

2.3.4.1 Principles of APT

The concept of atom probe tomography evolved from the field ion microscope, which first achieved imaging single atoms in 1955 by Erwin W. Müller at Pennsylvania State University.[18] This base technology relied upon the principle of field evaporation of atoms. A high voltage applied to a specimen is dramatically amplified at the sharp tip of the sample, which in turn ionizes surface atoms. The ionized atoms are ejected from the sample and recorded after striking a phosphor screen. The field ion microscope was then upgraded to a simple atom probe with the addition of a time-of-flight mass spectrometer, which is capable of detecting the identity of an ionized atom. The identity of an individual atom is determined by the following relationship:

$$\frac{m}{n} = 0.1928796(V)\frac{t^2}{d^2}$$

where m is mass, n is the number of electrons removed by the field ionization, V is voltage, d is distance between specimen and detector and t is the time of flight. The constant in this equation is dependent on the choice of voltage units; the shown constant is for voltages expressed in kilovolts.[18] This setup is deemed the one-dimensional atom probe. M.K. Miller then furthered the atom probe into the basic modern tomographic atom probe (TAP). The three-dimensional atom probe adds the additional information of

position-sensitive detectors. A diagram of the critical components of the TAP is shown in Figure 8.

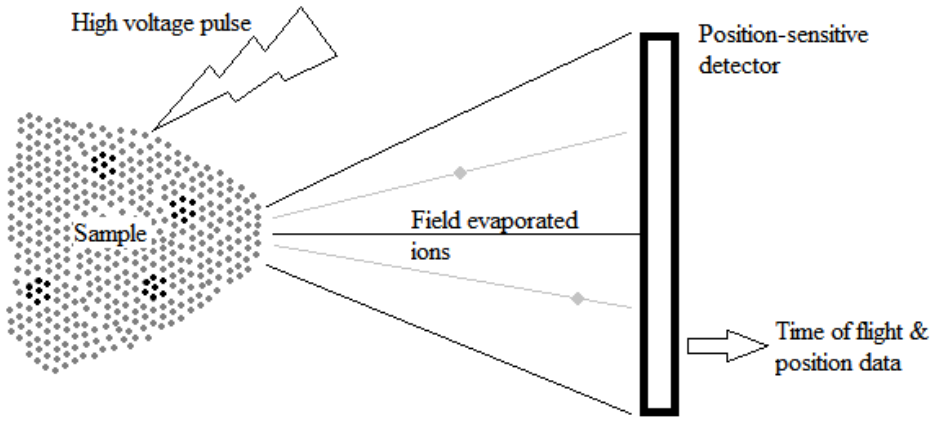

Figure 8 - Tomographic atom probe diagram

Coupling between the time-of-flight mass spectrometer and the position-sensitive detector allows post-processing software to reverse-construct the sample, which can be reconstructed into 3D models of the sample at the atomic level. The first quantitative TAP and the concept of an optical tomographic atom probe were developed at the Groupe de Physique des Matériaux (GPM) at Université du Rouen, France. The resolution of the position in modern machines can be as small as tens of nanometers under ideal conditions.[19] The specimens in this investigation were all studied with a Cameca FlexTAP with laser assistance and wide angle detector (LA-WATAP), as shown in Figure 9, at GPM.

Figure 9 - Cameca LA-WATAP tomographic atom probe

The laser assistance improves accuracy of the energy pulses that ionize the surface atoms, and the wide angle allows for a larger sampling region in the specimen. The specimens were analyzed at cryogenic temperatures in a near vacuum with a green laser and a detector diaphragm angle of 18 degrees. The data were then post-processed and constructed into 3D models with proprietary software developed by GPM.

2.3.4.2 Sample Preparation for APT

The sample preparation begins with production of a base holder in which the sample is later attached. A standard stainless steel insect pin is set in a nickel capillary tube by crimping, leaving approximately half a centimeter to a centimeter exposed on one end. The rest of the pin is removed so that the nickel tube will securely fit into the specimen holder in the APT apparatus. The needle is then sharpened to a very fine point by electropolishing under a microscope with a solution of perchloric acid and acetic acid. The voltage was varied between 5-15V as necessary to produce the desired tip. The tip required an extremely acute angle in preparation for the next step. A silicon post, with a nominal diameter of 5 microns, is attached to the tip of the sharpened pin with a two-part

conductive epoxy using an optical microscope with a micromanipulator apparatus. The post is glued in such a way that it is aligned with the longitudinal axis and approximately half of it extends beyond the tip. After the epoxy is cured, a small portion of the sample material is attached to the end of the silicon post using a micromanipulator. For the samples prepared for this investigation, the small pieces were formed from using a mortar and pestle to create powder. Powder particles that were slightly larger than the silicon post were selected so that the subsequent milling process was shortened. After the epoxy is cured, the sample(s) are introduced into a scanning electron microscope (SEM) that has a focused ion beam (FIB) device. The specimen particle is then linearly milled using the FIB to remove any large portion of the sample that overhangs the silicon post. Annual milling with the FIB is then used to sharpen the sample until a superfine point (tip radius of ~50nm) of the relevant material is created. A SEM image of an APT tip ready for analysis is shown in Figure 10. The image only shows the sample material at the tip and the silicon post, with a thin layer of the conductive epoxy in between.

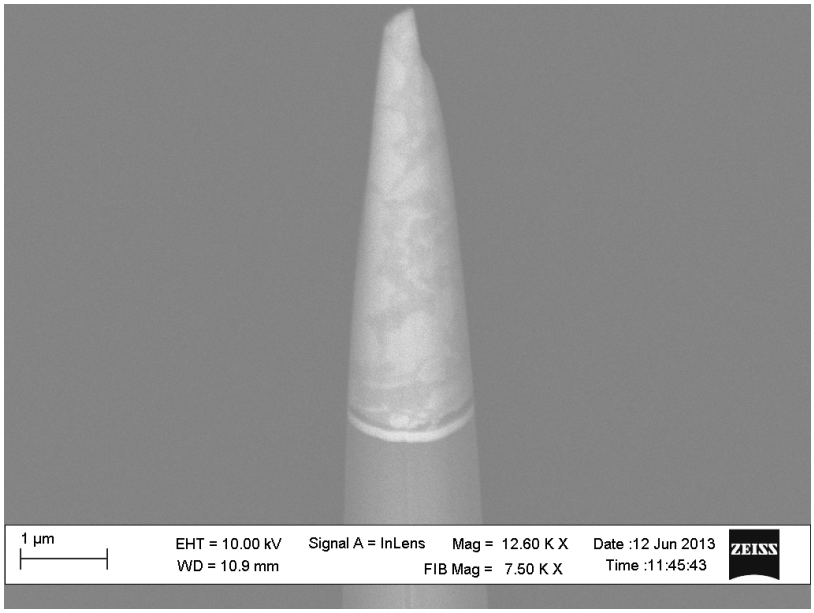

Figure 10 - Completed APT sample tip

Following the successful annular milling, the sample is ready for installation in the storage section of the device before transfer to the analysis chamber in the TAP.

Chapter 3:
RESULTS AND DISCUSSION

3.1 $HfCo_7$ Alloy

3.1.1 Structural Results

The $HfCo_7$ alloy served as the standard for comparison with the samples with substitutions, and therefore, was investigated initially. The samples were subjected to x-ray diffraction (XRD) analysis as single ribbons on both sides, designated as free-side and wheel-side. The sample was reported as having an orthorhombic structure with space group C222 with lattice parameters: a = 4.7189 Å, b = 4.2783 Å, and c = 8.0705 Å.[13] This was used as the expected structure in the investigation. The sample was initially examined on the wheel-side of the ribbon, with the resulting XRD pattern shown in Figure 11. Also, the major peaks are indexed with the appropriate (*hkl*).

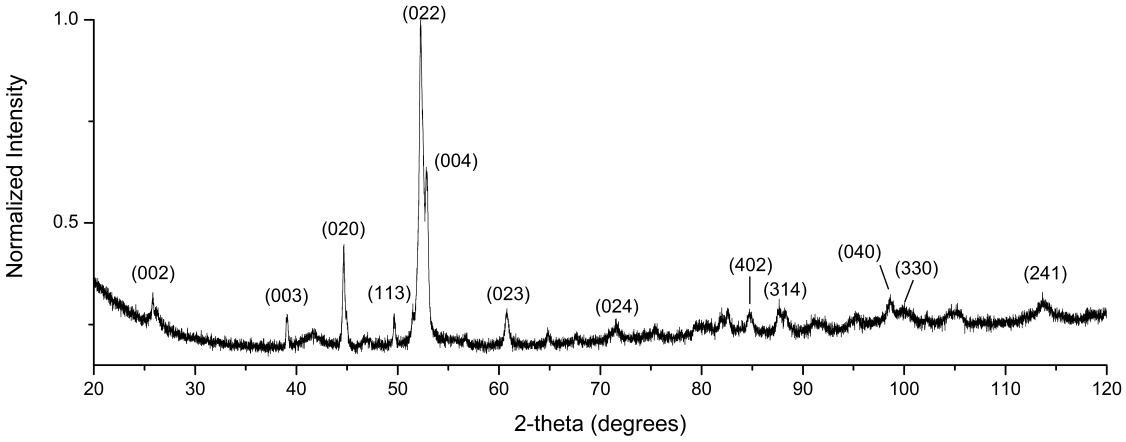

Figure 11 – XRD pattern for HfCo7 ribbon on wheel-side with major peaks indexed.

A cell-refinement program, CELREF V3, was used to analyze the peak positions through an iterative process to determine unit cell parameters. The calculated unit cell parameters

were a = 5.376 Å, b = 4.716 Å, and c = 8.029 Å (±0.001Å) for the C222 orthorhombic. These values are close to the values reported by Balamurugan, et al. However, the unit cell for this investigation is larger overall, with marginally larger values for parameters a and b.

The XRD patterns for the $HfCo_7$ sample on each side are shown in Figure 12. The two patterns are very similar with the only difference being the relative peak intensities. Additionally, adjusted cell parameters with the use of CELREF V3 refinement program are extremely similar. However, it should be noted there is a strong indication of texture in the (00ℓ) direction. The (002), (003) and (004) peaks have been marked in Figure 12 and shows a dramatic increase in intensity for the free-side measurement.

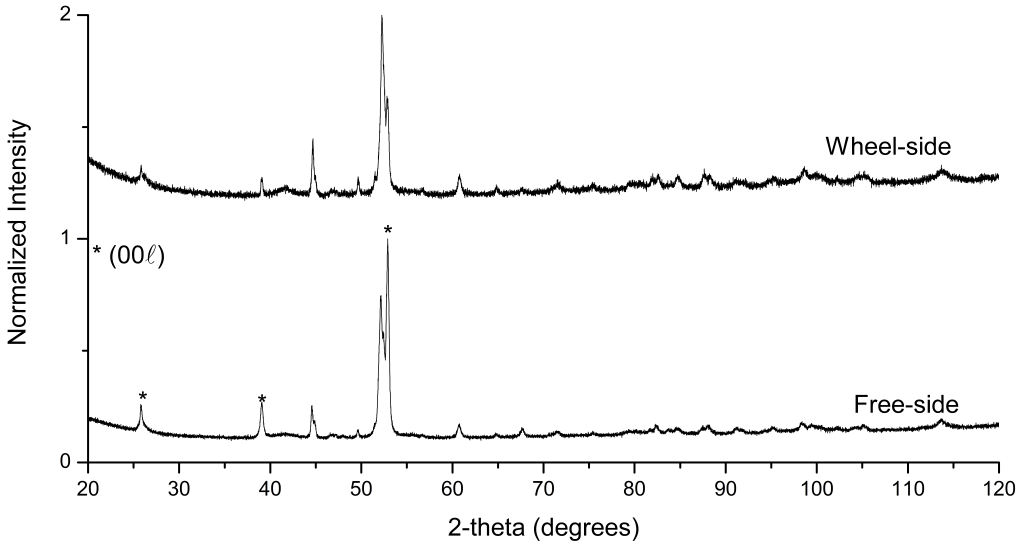

Figure 12 - XRD patterns for HfCo7 ribbons on the wheel & free sides.

The low wheel speed during melt spinning generally is more prone to differing solidification conditions for each side of the ribbon. The low speed led to directional solidification. Furthermore, the analysis of a ribbon instead of powder allows

investigation into the potential texture of the bulk material. Consequently, texture in the (00ℓ) direction is found on one side of the ribbon (free-side), as shown by the XRD data.

The $HfCo_7$ phase is a metastable intermetallic compound. This phase only can occur at the concentration indicated in the phase diagram (Figure 3). The phase is also metastable below 1050°C and would not exist at room temperature if cooled extremely slowly. The composition would rather form both Co (α) and Co_7Hf_2 phases. Thus, in order to form the target phase, the alloy must be overcooled within a particular range of kinetic conditions. The $HfCo_7$ phase was observed when following the aforementioned conditions for melt spinning. Hence, these conditions were used throughout this investigation.

The structure $HfCo_7$ alloy sample was further analyzed with the tomographic atom probe (TAP). The TAP is capable of sample reconstruction at the atomic level. The full sample tip is shown in Figure 13. After sample preparation described in Chapter 2, the reconstructed image showed areas of nearly pure cobalt, which is represented by the regions labeled as 90% isoconcentration (a feature of the data visualization software that bounds regions with >90% Co atoms, as shown in Figure 13). The $HfCo_7$ compound is observed in terms of relative proportion in the atom probe sample in the regions not indicated by the isoconcentration image.

The atom probe tomography images are difficult to represent as a full bulk, three-dimensional illustration due to the very large number of atoms presented in the data (5-10 million atoms). Hence, to provide a better representation of the sample, a 2-dimensional slice (approximately 10Å) is shown in Figure 14.

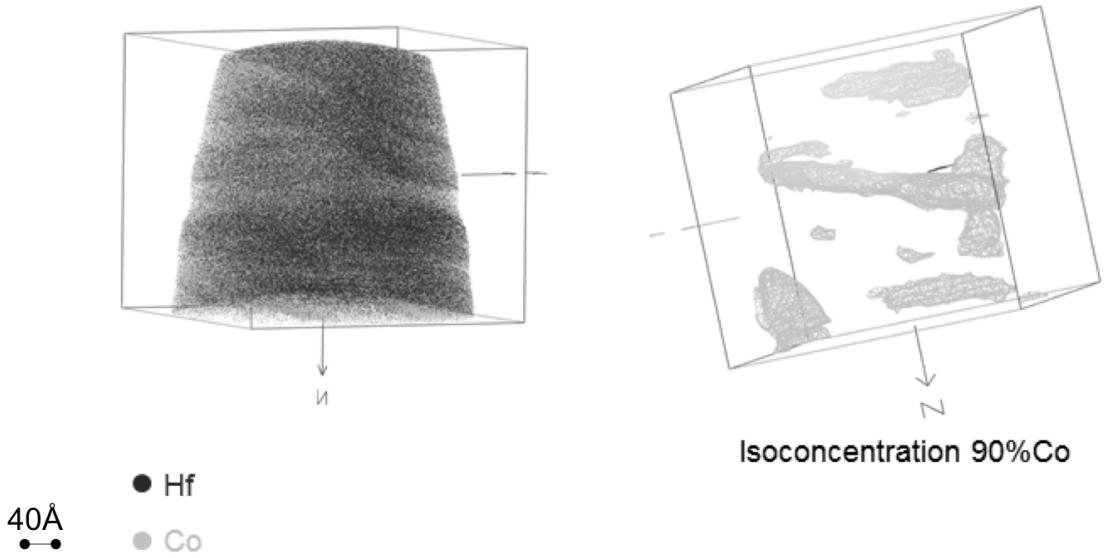

Figure 13 - Atom probe tomography results for HfCo7 with isoconcentration of Co.

Figure 14 - Tomographic atom probe 2D slice of HfCo7.

The 2D slice of the sample shows several regions of pure cobalt, indicated by the darker shaded regions that are approximately 30Å thick. Additionally, atomic planes are easily visible throughout the image, in particular on the central, right-hand side. The post-processing software used to visualize the TAP data also allows concentration calculations to be performed on the entire sample. The global concentration of the sample was found to be 86.4% cobalt atoms, which indicates the sample examined in the TAP is representative of the initial composition (nominally 87.5% Co atoms). The calculated atomic percentage of the non-cobalt rich regions was 85.8% Co. This value is slightly below the nominal composition and is a result of cobalt segregation into the secondary phase. This secondary pure cobalt phase comprises approximately 10% of the total sample volume. The small discrepancy between nominal and experimental results comes from the relatively minute size of the sample area and variations with the ribbons themselves. However, the results are close enough to be considered representative of the bulk material along with agreement in XRD results.

3.1.2 Magnetic Results

In terms of magnetic properties, the $HfCo_7$ sample was examined to a greater extent than the other samples as a standardized sample. The sample was measured in the in-plane-parallel, in-plane-perpendicular, and out-of-plane orientations in order to investigate the effect of shape anisotropy. From this, the optimal configuration for magnetic measurements can be determined. The orientation convention for the three tested directions is shown in Figure 15. Additionally, to isolate shape factors and determine possible microstructural differences, a square shaped sample was produced and measured in the SQUID magnetometer.

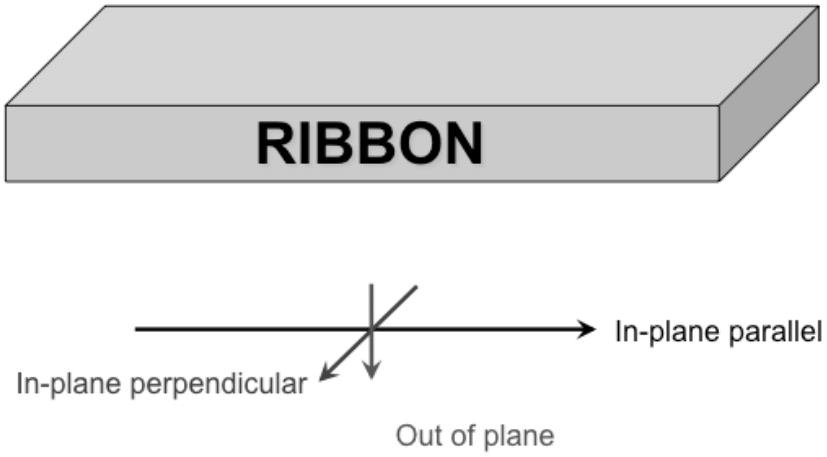

Figure 15 - Orientation convention for magnetic measurements.

It was determined that the in-plane-parallel orientation exhibited the truest magnetization and could effectively be used to test the actual magnetic properties of the alloy in question. The in-plane-parallel direction is measured as having the highest magnetization, as well as the fastest rate of saturation (Figure 16). The other orientations are limited in the displayed magnetization due to the anisotropy field from microstructure. The preferential direction of magnetization, or easy axis, appears to be in the in-plane-parallel direction. Additionally, the crystalline texture found on the free-side of the ribbons support the difference in susceptibility. In Figure 16, the lack of complete saturation in the sample indicates a larger applied field would be necessary to overcome the anisotropy field. The full loops for a sample (with an approximate size of 2.5mm x 0.75mm x 50μm) presented in Figure 16 were measured at 5K.

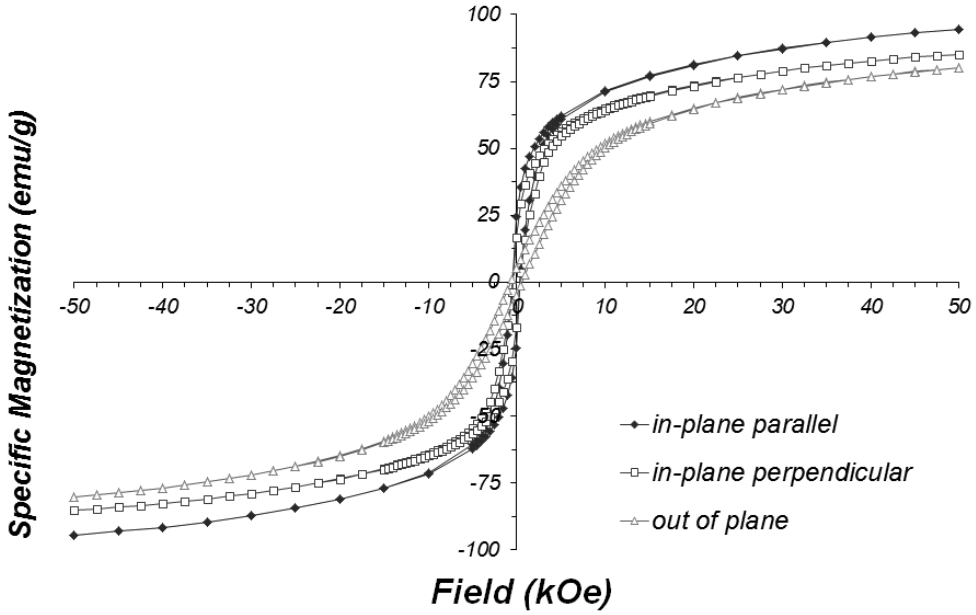

Figure 16 - Full loop SQUID measurements for different ribbon orientations (~2.5mm x 0.75mm x 50µm).

In order to exclude any macroscopic demagnetization effects due to sample shape, an effectively square piece of ribbon (750µm x 750µm x 50µm) was measured at 5K for half loops in a SQUID magnetometer. The in-plane-parallel orientation again exhibited the highest volume magnetization, as shown in Figure 17. The difference in recorded behavior between in-plane orientations is very small, but still indicates possible grain elongation in the ribbon long-axis (in-plane-parallel). The grain elongation is additionally supported by the texture found in the XRD patterns. However, as a result that the (00ℓ) texture only appears on one side of the ribbons and is not prevalent throughout the sample, the effects due to grain elongation are minimal. Thus, the easy axis of magnetization is assumed to be in the in-plane-parallel direction.

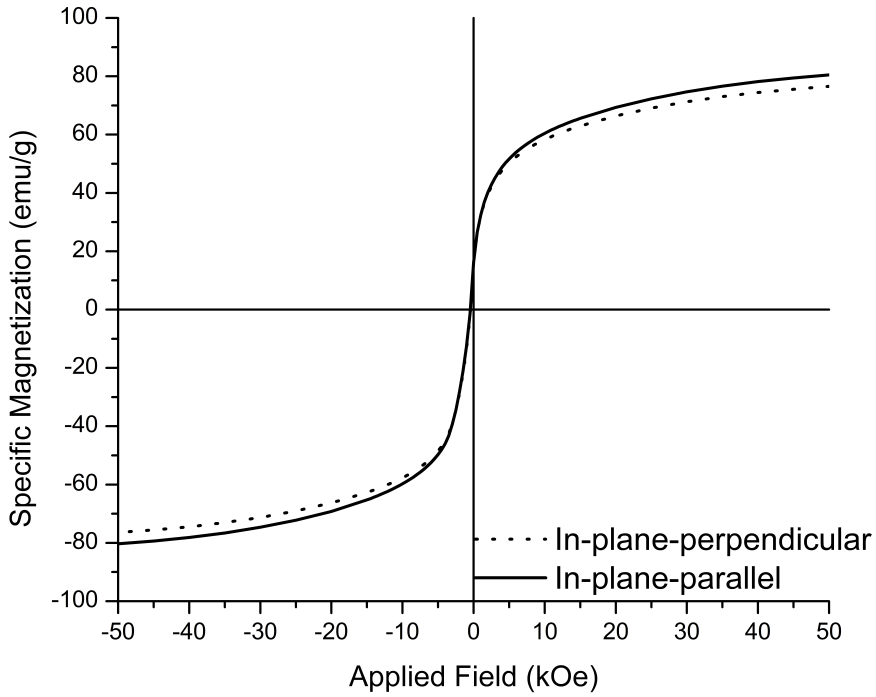

Figure 17 - Magnetization of HfCo7 square sample (750µm x 750µm x 50µm) (1/2 loops).

As a result of the orientation results, all magnetic measurements that follow are in the in-plane-parallel configuration, unless otherwise noted.

The $HfCo_7$ samples were also subjected to experiments to determine the effects of temperature on magnetic properties. A temperature sweep was performed at 25 kOe from 5K to 400K. The normalized moment (raw measurement data from the SQUID) as a function of temperature is shown in Figure 18 (note: a drop in temperature during the scan occurred at around 275K, but does not effect results of scan). The sample exhibits a loss of around 5% between 5K and 400K, indicative of the high Curie temperature of the compound. However, the SQUID is incapable of measurements higher than 400K, which is not close to the reported value of 600K.[10] Therefore, the Curie temperature cannot be determined with the equipment utilized.

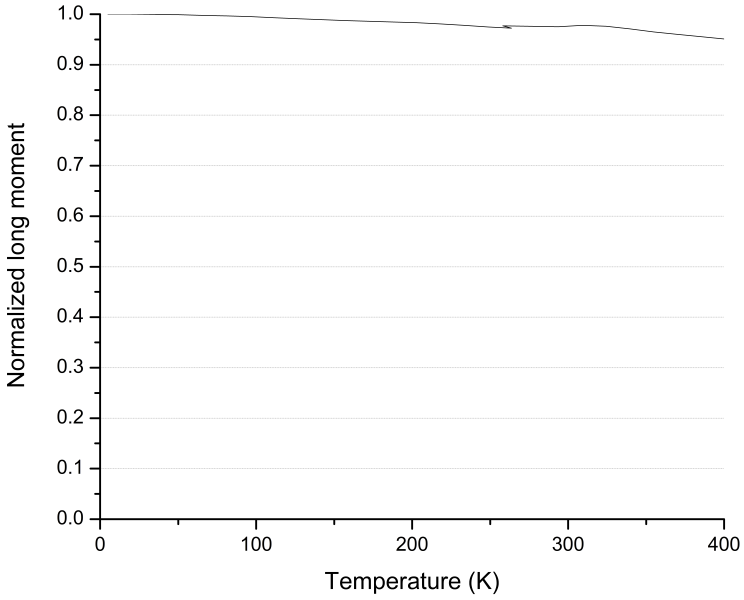

Figure 18 - Temperature sweep from 5K to 400K for HfCo7 at 25 kOe (H = 25 kOe).

For comparison to other materials, the magnetic results must be quantified in specific magnetization, or magnetization per unit mass, rather than qualitative measurements. The SQUID results for $HfCo_7$ ribbons at 5K (representative of near optimal conditions) and 300K (representative of room temperature) are shown in Figure 19. The magnetization at H = 50 kOe is approximately 95 emu/g and 80 emu/g for 5K and 300K, respectively. The coercivity of the $HfCo_7$ sample is very low, ~0.4 kOe for both temperatures, indicating a semi-hard magnetic material.

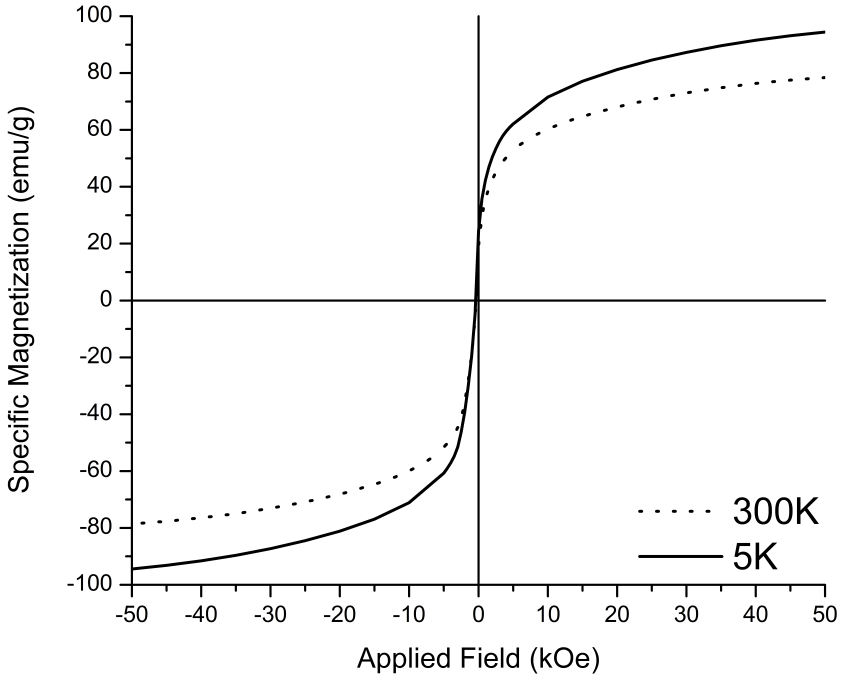

Figure 19 - Specific magnetization for HfCo7 at 5K & 300K (1/2 loops).

3.2 Substitutions with Silicon & Titanium

Samples containing silicon and titanium substitutions had the following atomic compositions: $HfCo_{6.5}Si_{0.5}$, $HfCo_6Si$, $HfCo_{6.75}Ti_{0.25}$ and $HfCo_{6.5}Ti_{0.5}$. The substitution elements are used to alter either the intrinsic or extrinsic magnetic properties. For atoms that enter the primary phase, the intrinsic properties such as saturation magnetization and Curie temperature can be changed.[20] On the other hand, the extrinsic properties, such as remanence and coercivity, are influenced by the morphology of the material. Primarily, this is realized by the formation of an additional phase(s). The Si and Ti substitutions had comparable effects on the $HfCo_7$ alloy.

3.2.1 Structural Results

The silicon samples resulted in a gradual loss of the orthorhombic phase with increasing Si content. The XRD patterns for $HfCo_{6.5}Si_{0.5}$ and $HfCo_6Si$ are shown in Figure 20. The peaks associated with the orthorhombic phase are present in the $HfCo_{6.5}Si_{0.5}$ sample along with an additional phase(s). The phase(s) found in the $HfCo_6Si$ specimen are complex and difficult to identify.

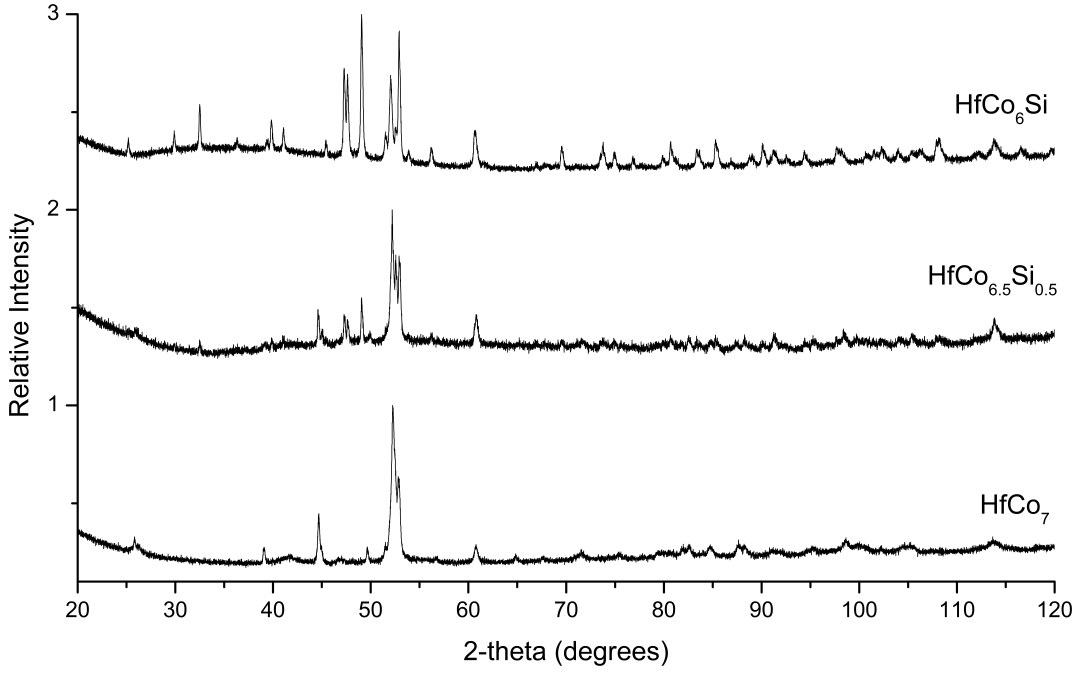

Figure 20 - XRD patterns for silicon substitution samples.

Titanium substitutions in the $HfCo_7$ system similarly lead to a loss of the orthorhombic phase with increasing concentration. The XRD patterns for the $HfCo_{6.75}Ti_{0.25}$ and $HfCo_{6.5}Ti_{0.5}$ are presented, alongside the binary pattern, in Figure 21. The $HfCo_{6.75}Ti_{0.25}$ sample had relatively low phase fraction of the orthorhombic structure. However, the orthorhombic phase is no longer detectible in the $HfCo_{6.5}Ti_{0.5}$ sample. Additional peaks

can be seen in the $HfCo_{6.75}Ti_{0.25}$ alongside the 1:7 phase, indicating a multi-phase microstructure.

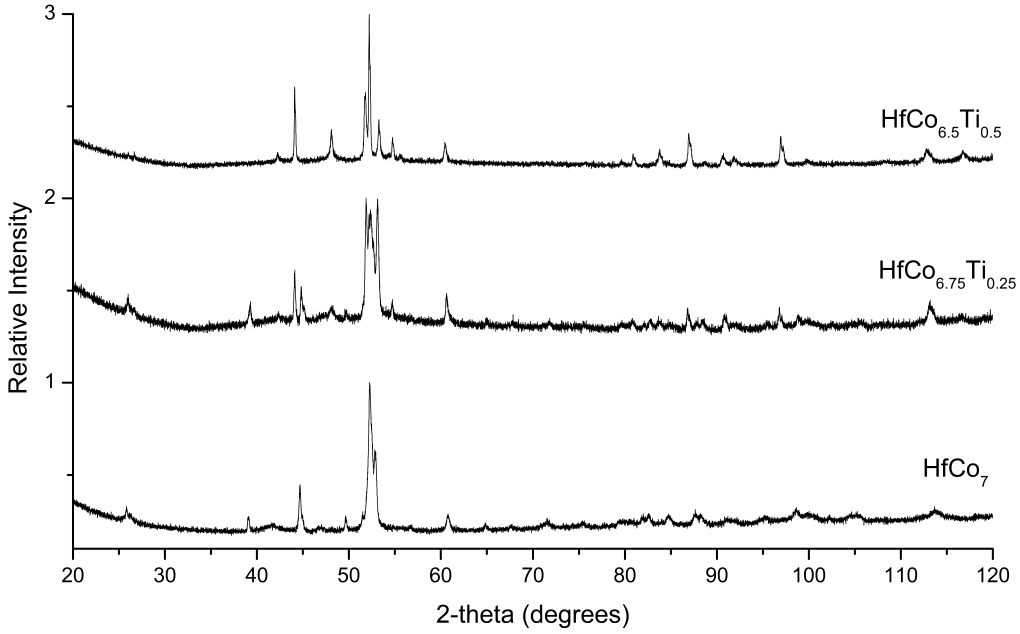

Figure 21 - XRD patterns for titanium substitution samples.

3.2.2 Magnetic Results

The magnetic measurements for the silicon and titanium samples are presented in Figure 22 and Figure 23, respectively. These samples show a large decrease in magnetization at 50 kOe compared to the binary alloy. The samples with a multi-phase system ($HfCo_{6.5}Si_{0.5}$ and $HfCo_{6.75}Ti_{0.25}$) showed a reduction in magnetization and susceptibility due to smaller proportion of magnetic phase. The other samples that did not form the orthorhombic phase ($HfCo_6Si$ and $HfCo_{6.5}Ti_{0.5}$) saturate at low fields with a lower magnetization than the substitution-free sample. The substitutive atoms enter the orthorhombic structure and lead to a reduction of magnetic saturation. This is because neither Si nor Ti atoms can carry a magnetic moment, causing a reduction the overall magnetization.

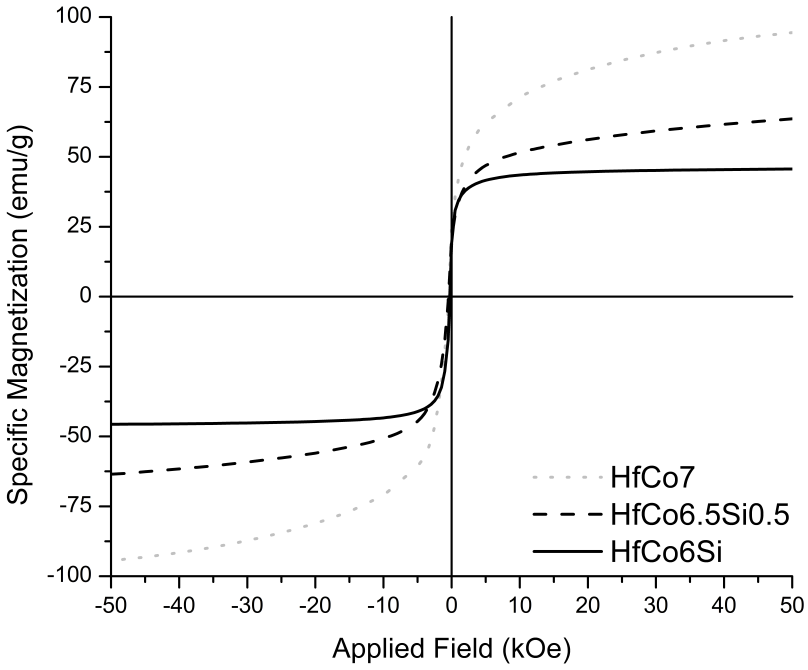

Figure 22 - Magnetization for silicon samples at 5K (1/2 loops).

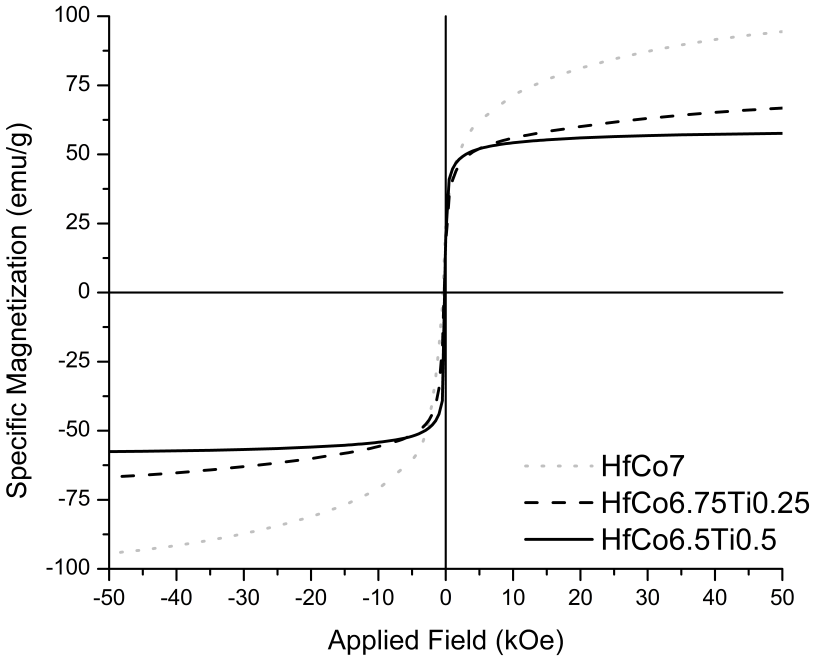

Figure 23 - Magnetization for titanium samples at 5K (1/2 loops).

3.3 Substitution with Iron

The hafnium cobalt 1:7 phase was also altered with substitutions of iron. These samples were created with the atomic ratios of $HfCo_{6.5}Fe_{0.5}$ and $HfCo_6Fe$.

3.3.1 Structural Results

The XRD results for the iron substitution samples are presented alongside the binary alloy pattern in Figure 24. The $HfCo_{6.5}Fe_{0.5}$ sample produced a pattern consistent with the orthorhombic structure with minor shifts in peak positions. For the $HfCo_6Fe$ sample, this phase is faintly present with low intensity peaks. The relatively stronger peaks in the pattern have been indexed to the $HfCo_2$ binary phase and the α-Co (face-centered cubic, FCC) phase. These two phases seem to dominate the pattern. It is interesting to note, the $HfCo_2$ phase has been reported as paramagnetic at 5K.[21] However, the retention of the orthorhombic phase for the $HfCo_{6.5}Fe_{0.5}$ specimen with shifted peaks indicates iron atoms enter into the phase, creating small changes in the unit cell dimensions.

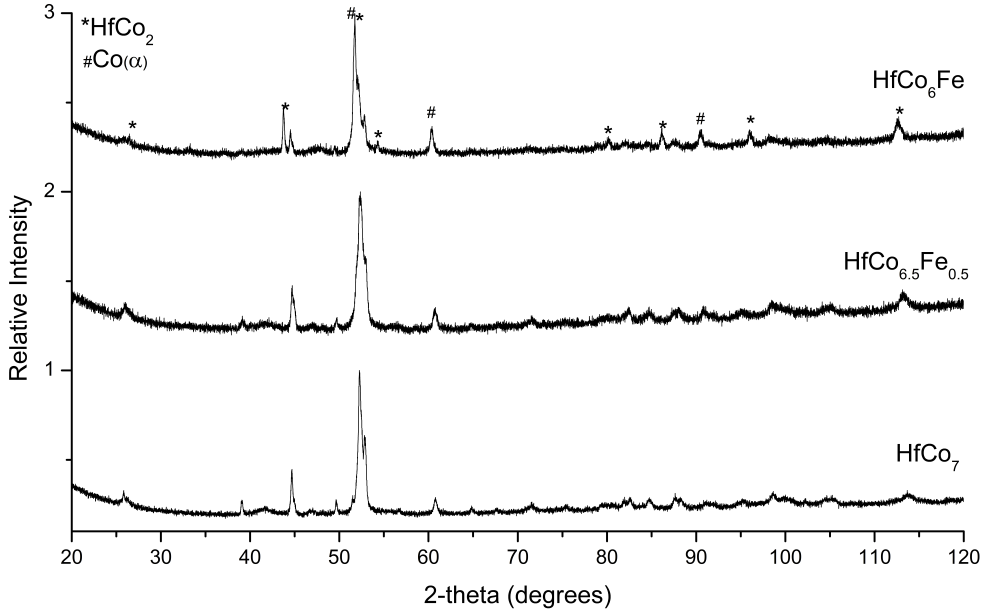

Figure 24 - XRD patterns for iron substitution samples.

3.3.2 Magnetic Results

These samples only were subjected to ±10 kOe applied field. The binary alloy reached a comparable magnetization (~62 emu/g) at 10 kOe as tested at previously (~70 emu/g). Therefore, the data is expected to correctly represent the magnetic response of the materials and supports the sample. The iron samples have a higher magnetic susceptibility. The sample does not saturate completely, but appears to approach a similar saturation limit as the binary alloy. Additionally, the coercivities do not differ much between the three samples.

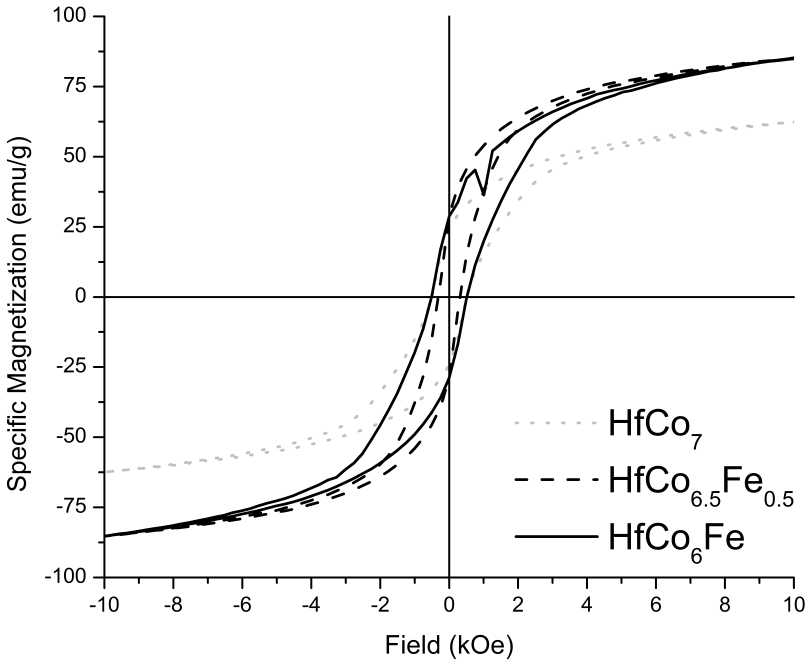

Figure 25 - Magnetization for iron samples at 5K from -10kOe to 10kOe.

3.4 Substitution with Manganese

The samples containing manganese consisted of the elemental compositions $HfCo_{6.5}Mn_{0.5}$ and $HfCo_6Mn$, which follow the formula $HfCo_{7-x}Mn_x$.

3.4.1 Structural Results

The x-ray diffraction patterns for both manganese samples are displayed in Figure 26. The two manganese-containing compositions produced similar XRD patterns. However, the structure was not consistent with the structure of the $HfCo_7$ binary alloy. Therefore, the manganese substitutions formed a distinct phase(s) that had not been reported in international diffraction databases for this ternary system.

The $HfCo_{6.5}Mn_{0.5}$ pattern has a slight indication of an amorphous region within the sample as indicated by the halo in Figure 26. The amorphous halo was not present in the XRD pattern for $HfCo_6Mn$. Therefore, this specific composition could be closer to the exact proportion needed to form the distinctive phase or multiple phases could have been formed. As a result of both broad and sharp peaks in the pattern for $HfCo_6Mn$, it is likely that at least two phases exist in the sample (neither of which is the orthorhombic phase). For $HfCo_6Mn$, the $HfCo_2$ and α-Co phases were evident (Figure 26); additionally, other peaks not consistent with previously reported relevant compounds. Thus, this alloy consists of at least three phases.

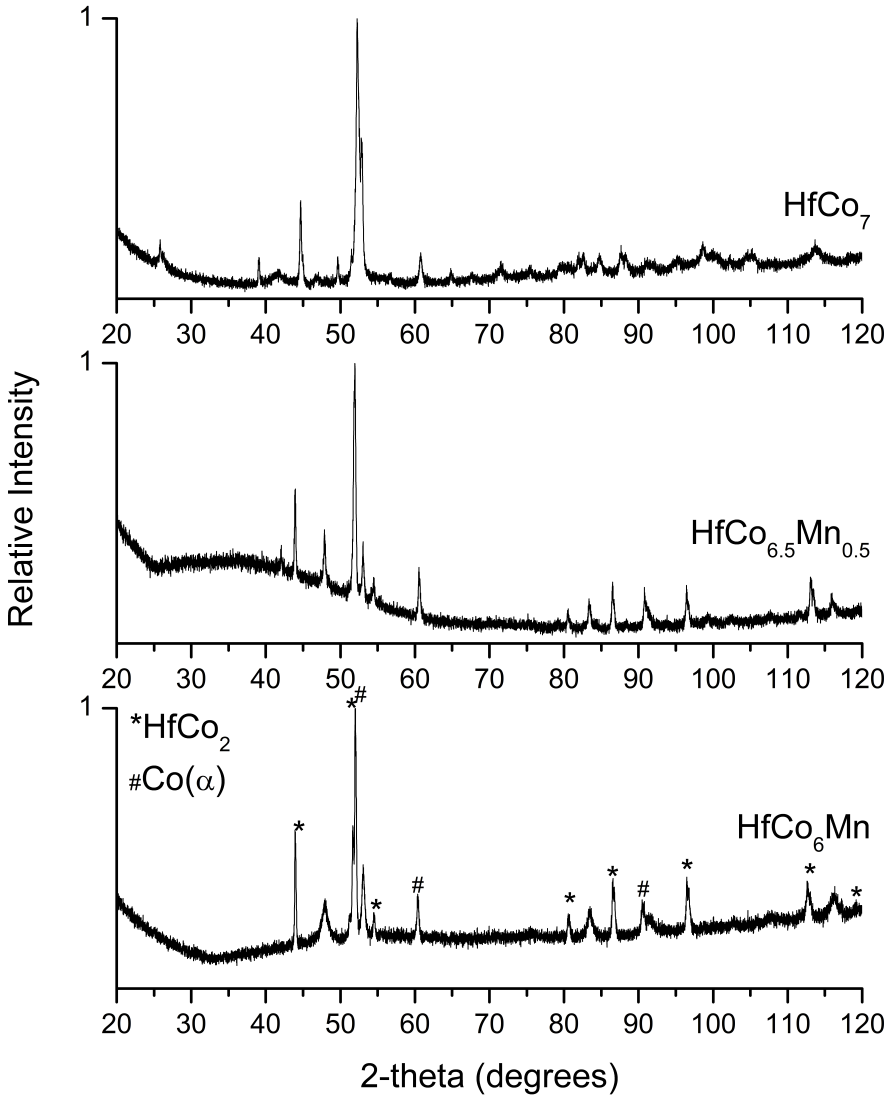

Figure 26 - XRD patterns for manganese samples.

3.4.2 Magnetic Results

The manganese-containing samples were magnetically analyzed in a SQUID magnetometer to produce the half-loops presented in Figure 27. The addition of manganese resulted in a reduction of coercivity in the samples compared to the binary alloy. The manganese alloys are effectively soft ferromagnetic materials.

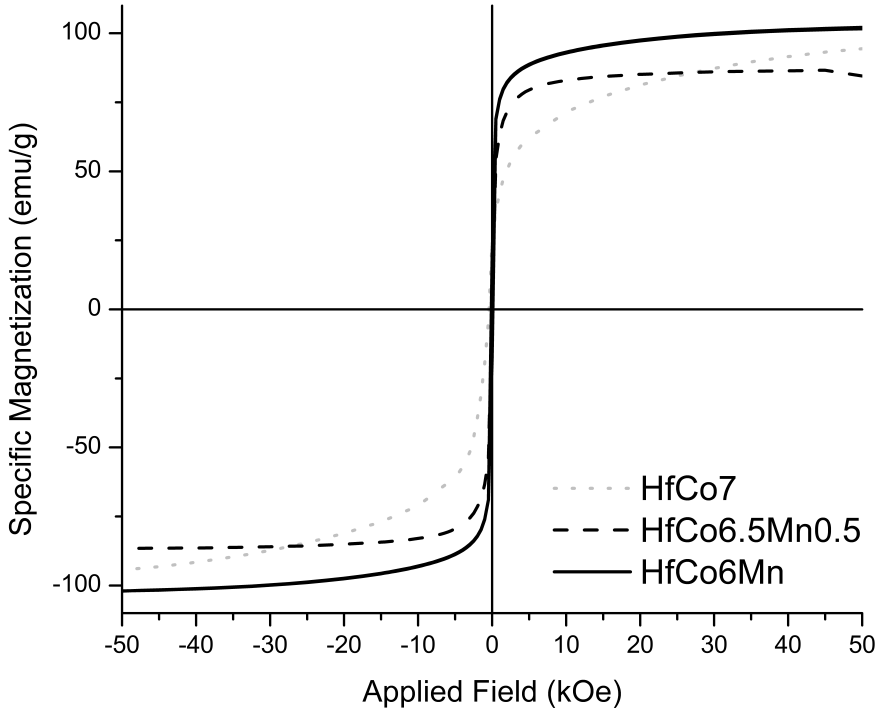

Figure 27 - Magnetization for manganese samples at 5K (1/2 loops).

The manganese samples had a higher susceptibility than the $HfCo_7$ alloy. The magnetization at 50 kOe value was slightly reduced from the initial compound (94.4 emu/g) to 84.5 emu/g for the x = 0.5 sample. The $HfCo_6Mn$ sample not only demonstrated a greater susceptibility, but also presented an increased magnetization at 50 kOe of 101.65 emu/g.

The values mentioned were obtained during tests at 5K and were not stable at higher temperatures. The phase formed from the $HfCo_6Mn$ composition was further explored in its magnetic stability over the temperature range of 5K to 400K, as illustrated in Figure 28. The material only demonstrated 80% of the magnetic moment at room temperature compared to 5K, and nearly an additional 10% was observed to be lost at 400K (the limit

of the testing equipment). Thus, the magnetic phase formed in the manganese-containing samples is not stable at high temperatures like the $HfCo_7$ phase.

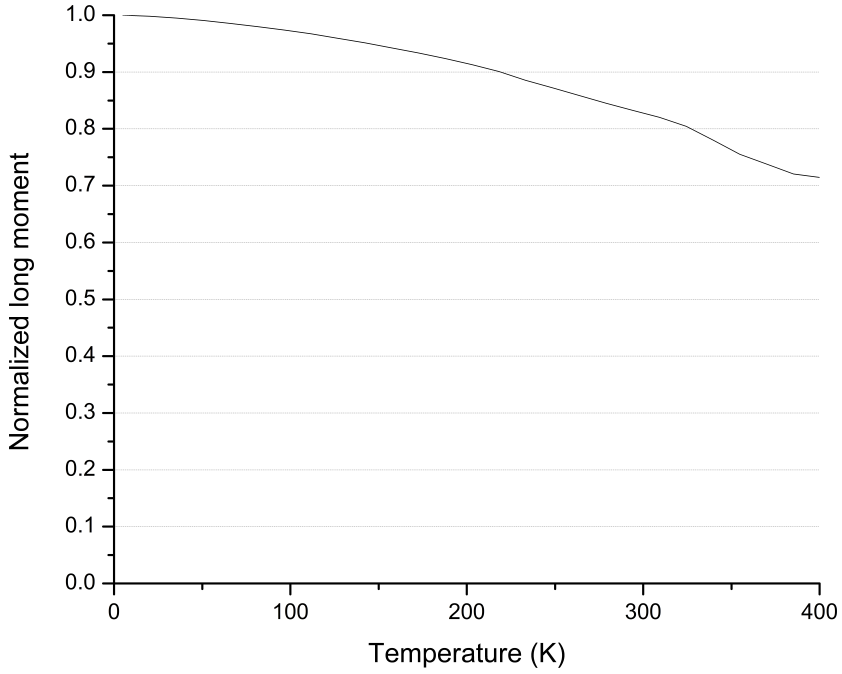

Figure 28 - Temperature stability of HfCo6Mn sample from 5K to 400K (H = 25 kOe).

3.5 Substitution with Boron

The original alloy composition was initially altered with boron substituting for cobalt. The original formula for substitution called for $HfCo_{6.5}B_{0.5}$ and $HfCo_6B$ samples. However, due to difficulties involved with arc melting boron, the $HfCo_6B$ sample was not successfully made. Instead, a loss of boron during the arc melting process, produced a sample more accurately represented by $HfCo_6B_{o.75}$. Thus, the samples analyzed with boron were $HfCo_{6.5}B_{0.5}$ and $HfCo_6B_{0.75}$.

3.5.1 Structural Results

The XRD patterns for $HfCo_{6.5}B_{0.5}$ and $HfCo_6B_{0.75}$ are presented in Figure 29. Both samples predominately show peaks corresponding to the orthorhombic $HfCo_7$ binary phase. However, there are several important distinctions to note for these samples. The patterns both have additional peaks, which indexed to the $HfCo_3B_2$ ternary phase. The peaks appear much more clearly in the $HfCo_6Hf_{0.75}$ pattern and are indicated with an asterisk (*) in Figure 29.

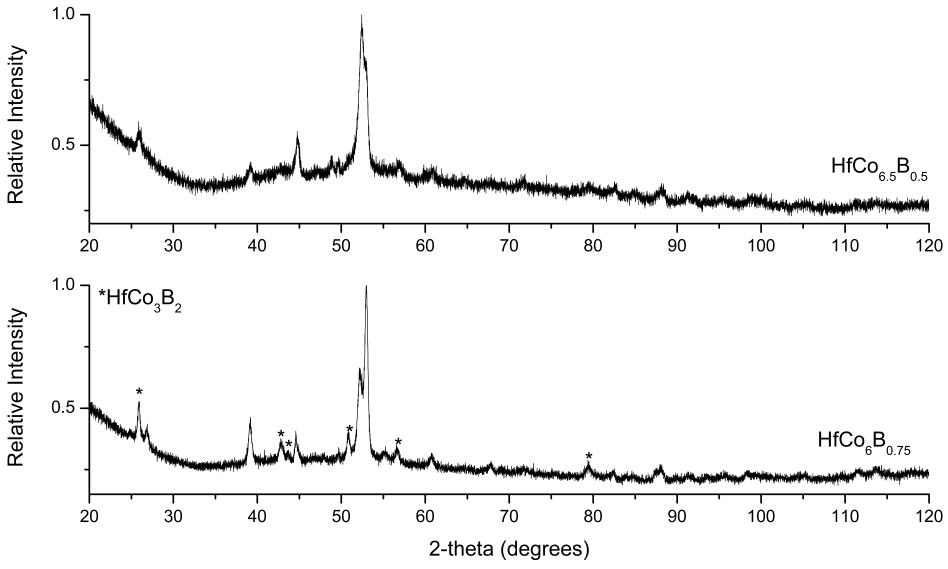

Figure 29 - XRD patterns for boron containing samples.

Furthermore, the patterns both exhibit a slight amorphous halo, which is more defined in the $HfCo_{6.5}B_{0.5}$. However, the amorphous halo is not large and thus suggests a relatively small portion of non-crystalline material.

In order to understand the microstructure of the specimens created, the samples were further examined in the tomographic atom probe. A slice representative of the entire TAP specimen is shown in Figure 30, along with a linear concentration profile. The

concentration profile shows the relative concentration of each element along the length of the arrow. Similar to the substitution-free sample, the $HfCo_{6.5}B_{0.5}$ is primarily the $HfCo_7$ phase with a few small regions of essentially pure cobalt. The boron has almost entirely segregated into a third region, which is the focus of the linear concentration profile. The profile shows essentially no boron in the $HfCo_7$ region, indicating boron atoms do not enter the primary phase, and the segregation leads to the formation of $HfCo_3B_2$.

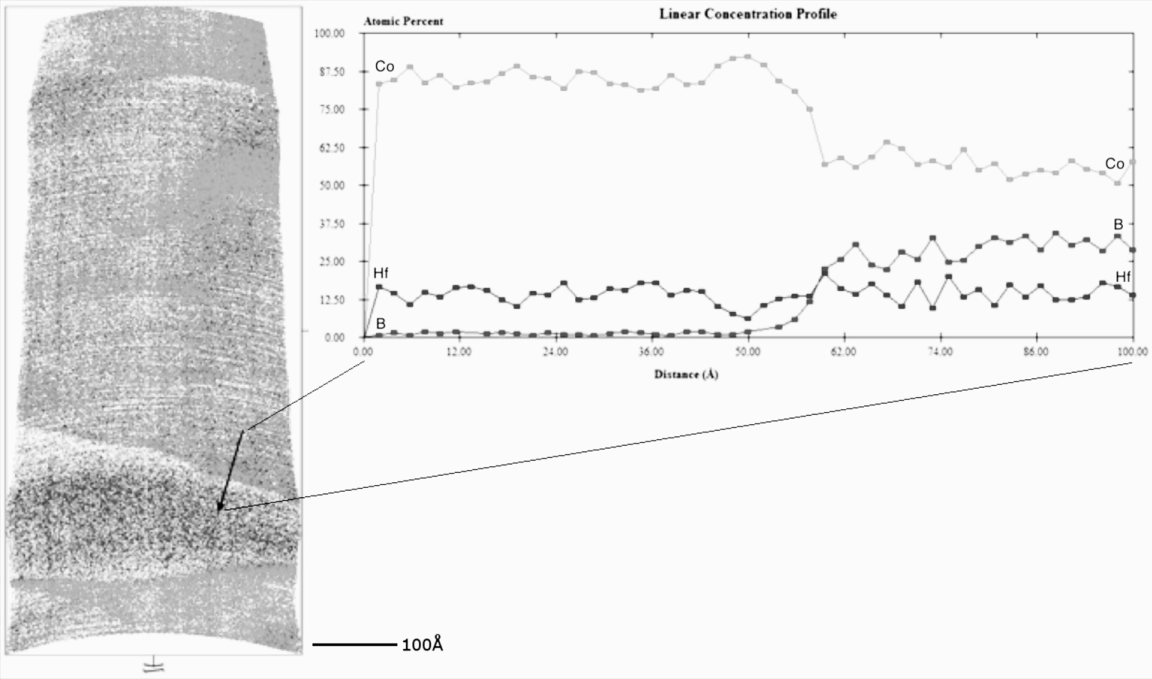

Figure 30 - TAP results for $HfCo_{6.5}B_{0.5}$ including linear concentration profile (along arrow).

The TAP results for the $HfCo_6B_{0.75}$ displayed a similar microstructure in terms of the boron distribution. However, a pure cobalt region was not observed in the specimen. Furthermore, the boron-rich regions formed a slightly greater phase fraction in comparison to the $HfCo_{6.5}B_{0.5}$ sample.

3.5.2 Magnetic Results

The magnetic measurement performed on the boron-substituted samples yields interesting results; specifically the coercivity is drastically improved from 0.4 kOe without boron up to 5 kOe for $HfCo_6B_{0.75}$. The magnetization, however, was drastically reduced by the addition of the boron. The half loops for both samples containing boron, as well as the base alloy, are shown in Figure 31. The coercivity increases with boron concentration; 3.12 kOe and 4.49 kOe for $HfCo_{6.5}B_{0.5}$ and $HfCo_6B_{0.75}$, respectively. However, the magnetizations at an applied field of 50 kOe were reduced by over a third in comparison to the original binary alloy from 94.4 emu/g to 68.0 emu/g for $HfCo_{6.5}B_{0.5}$ and 64.0 emu/g for $HfCo_6B_{0.75}$.

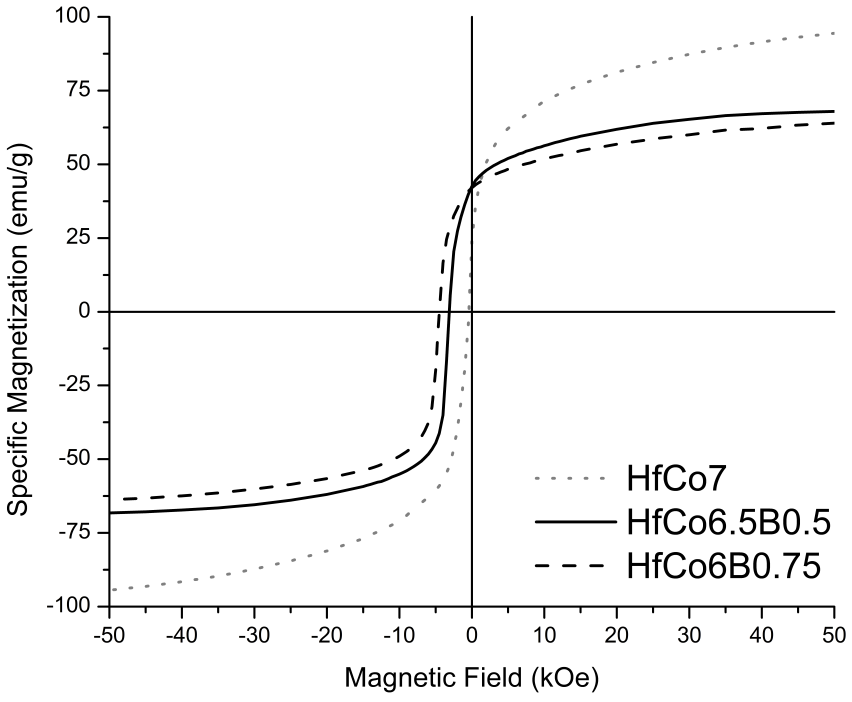

Figure 31 - Magnetization of boron samples at 5K (1/2 loops).

The reduction of magnetization was a result of overall proportion of ferromagnetic phases within the bulk material. The boron-rich phase did not contribute to the magnetism, and led to the observed loss. Yet, the $HfCo_3B_2$ effectively isolates $HfCo_7$ grains, reducing magnetostatic interactions and increasing coercivity.

The boron samples were examined magnetically at 5K and 300K, resulting in the hysteresis half-loops shown in Figure 32. The coercivity of samples was essentially unchanged between the temperatures. The saturation magnetization at 50 kOe was unchanged by temperature for the $HfCo_{6.5}B_{0.5}$ composition, while the other boron sample experienced a slight decrease. The resistance to temperature effects on magnetization parallels the $HfCo_7$ phase. This is further evidence of the active magnetic phase being the orthorhombic phase and suggests that the boron does not alter the magnetic properties of the phase itself.

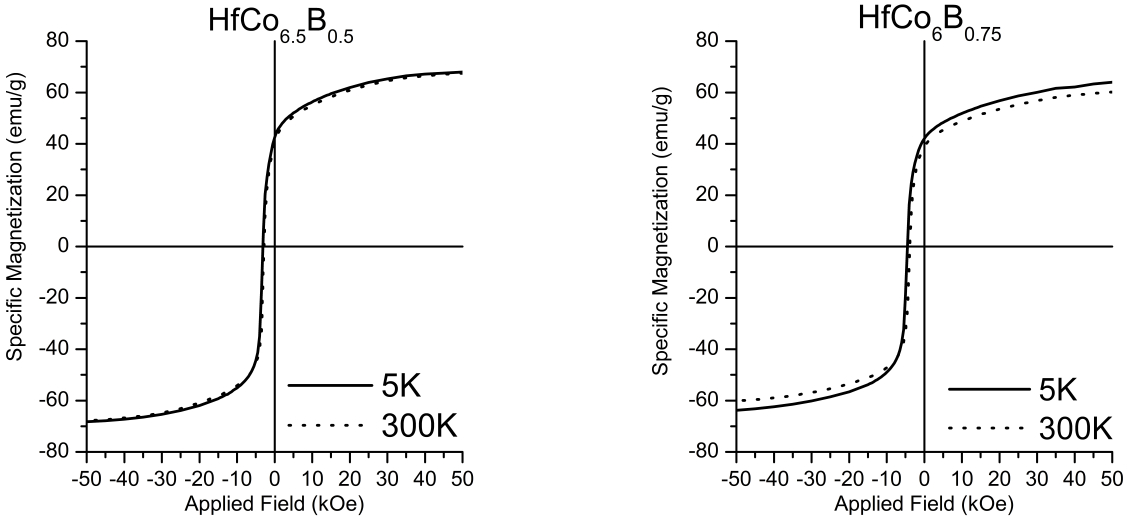

Figure 32 - Temperature effects on boron containing samples (1/2 loops).

Chapter 4:
CONCLUSIONS

The hafnium-cobalt alloy system was altered by substituting cobalt atoms with silicon, titanium, iron, manganese and boron at various concentrations. The samples included $HfCo_7$, $HfCo_{6.5}Si_{0.5}$, $HfCo_6Si$, $HfCo_{6.75}Ti_{0.25,}$ $HfCo_{6.5}Ti_{0.5}$ $HfCo_{6.5}Mn_{0.5}$, $HfCo_6Mn$, $HfCo_{6.5}B_{0.5}$ and $HfCo_6B_{0.75}$. All the samples were created under the same experimental conditions in order to focus on the effects of the substitution element.

The binary alloy was observed to have a specific magnetization at 50 kOe of 94.4 emu/g, or a volumetric M_s of 761 emu/cm^3, which exceeds the reported values. However, the observed coercivity of 0.42 kOe is much lower than the value reported in the literature. The higher magnetization is probably related to the pure-cobalt regions found in the atom probe tomography results. While the Curie temperature was not verified, the magnetic stability was corroborated up to 400K.

The structure of the $HfCo_7$ alloy was identified as a two-phase compound of $HfCo_7$ intermetallic phase with orthorhombic structure and pure cobalt. The orthorhombic structure (space group C222) was determined to have unit cell parameters of a = 5.376 Å, b = 4.716 Å, and c = 8.029 Å. These are consistent with previous reports of structure. The XRD patterns showed the samples had directional solidification with texture in the (00ℓ) direction on the free-side. The formation of the cobalt pure phase could be a result of production conditions and requires additional investigation to determine the cause. Substitutions of silicon and titanium changed the phase relationships and significantly reduced magnetization at 50 kOe. Additionally, these samples had little affect on the

coercivity. The iron substituted samples also showed a decomposition of the orthorhombic phase into $HfCo_2$ and α-Co phases with increasing iron content.

The substitution of manganese in the $HfCo_7$ alloy resulted in the formation of a new ternary phase. The unique phase was observed in both the $HfCo_{6.5}Mn_{0.5}$, and $HfCo_6Mn$ compositions. This phase was observed as having a higher magnetic susceptibility. Additionally, the magnetization at 50 kOe was 101.7 emu/g for the $HfCo_6Mn$ sample, which was greater than both the $HfCo_{6.5}Mn_{0.5}$ (84.5 emu/g) and the binary $HfCo_7$ alloy. However, the coercivity was very low and could be a result of microstructure. Therefore, this ternary alloy deserves further investigation to identify the structure.

The addition of boron to the alloy led to the development of a boron-rich region in both cases. The $HfCo_{6.5}B_{0.5}$ sample produced the same two phases as the binary alloy, the orthorhombic phase and the pure cobalt phase, along with $HfCo_3B_2$. However, the $HfCo_6B_{0.75}$ does not exhibit the cobalt phase. The presence of the non-magnetic phase reduced the magnetization at 50 kOe to 68.0 emu/g and 64.0 emu/g for $HfCo_{6.5}B_{0.5}$ and $HfCo_6B_{0.75}$, respectively, due to the smaller volume of ferromagnetic phases. The coercivity, however, was greatly improved for each sample. The coercivity of $HfCo_{6.5}B_{0.5}$ and $HfCo_6B_{0.}75$ was 3.12 kOe and 4.49 kOe, respectively. The increase in coercivity stems from the separation of magnetic grains.

The limited variations of the conditions leave several avenues of interest to be explored further by other investigators. The boron samples require further examination in microstructural refinement to reduce the boron-rich region, which could be achieved though varying conditions during the melt spinning and/or further processing. Furthermore, the structure of the manganese samples could be further explored with

additional post-production techniques. The effects on the $HfCo_7$ alloy can be further explored by altering substitution quantities, examining additions and/or material production methods.

REFERENCES

[1] Guimaraes A. P., 2005, From Lodestone to Supermagnets: Understanding Magnetic Phenomena, Wiley-VCH Verlag GmbH & Co. KGaA, Weinheim, Germany.

[2] Chu S., 2011, Critical Materials Strategy, U.S. Department of Energy.

[3] McCallum R. W., "Replacing Critical Rare Earth Materials in High Energy Density Magnets," The Ames Lab: Division of Materials Sciences and Engineering [Online]. Available: https://www.ameslab.gov/dmse/apra -e-projects/replacing-critical-rare-earth-materials-high-energy-density-magnets-main.

[4] Tse B. P., 2011, China's Rare-Earth Industry, U.S. Geological Society, Reston, Virginia.

[5] Lucis M. J., Wang M., and Shield J. E., 2013, "High Coercivity MnAl(C) Permanent Magnets," 58th Annual Conference on Magnetism and Magnetic Materials, Denver, CO, pp. 342–343.

[6] Obi O., Lucis M., Wang M., Chen Y., Shield J. E., and Harris V. G., 2013, "MnAlC/FeCo Exchange-Coupled Permanent Magnets," 58th Annual Conference on Magnetism and Magnetic Materials, Denver, CO, pp. 601–602.

[7] Cui J., Kramer M., Marinescu M., Liu P., Nguyen V., Huang Q., Choi J., Takeuchi I., Reeve H., Li G., Droubay T., Polikarpov E., Templeton J., and Darsell J., 2013, "Development of MnBi Permanent Magnet," 58th Annual Conference on Magnetism and Magnetic Materials, Denver, CO, p. 342.

[8] Jin Y., Zhang W., Skomski R., Shield J. E., and Sellmyer D. J., 2013, "Phase Composition and Nanostructure of Zr2Co11-Based Alloys," 58th Annual Conference on Magnetism and Magnetic Materials, Denver, CO, pp. 345–346.

[9] Demczyk B. G., and Cheng S. F., 1991, "Structures of Zr2Co11 and HfCo7 intermetallic compounds," Journal of applied crystallography, **24**(6), pp. 1023–1026.

[10] Buschow K. H. J., 1982, "Differences in magnetic properties between amorphous and crystalline alloys," Journal of Applied Physics, **53**(11), p. 7713.

[11] Skomski R., and Coey J. M. D., 1999, Permanent Magnetism, Institute of Physics Publishing, Bristol, UK.

[12] Ishida K., and Nishizawa T., 1991, "The Co-Hf (Cobalt-Hafnium) system," Journal of Phase Equilibria, **12**(4), pp. 424–427.

[13] Balamurugan B., Das B., Shah V. R., Skomski R., Li X. Z., and Sellmyer D. J., 2012, "Assembly of uniaxially aligned rare-earth-free nanomagnets," Applied Physics Letters, **101**(12), p. 122407.

[14] Prost T., 2012, "Magnetic Properties Study of the Mn-Al System with Additions of B or C and Mechanical Milling Techniques," University of Nebraska-Lincoln.

[15] Carelli P., and Paterno G., 1992, "Macroscopic Quantum Interference: DC-SQUID," Principles and Applications of Superconducting Quantum Interference Devices, A. Barone, ed., World Scientific Publishing Co. Pte. Ltd., Singapore, pp. 4–75.

[16] Clarke J., and Braginski A. I., 2004, The SQUID Handbook: Vol. I - Fundamentals and Technology of SQUIDs and SQUID Systems, Wiley-VCH Verlag GmbH & Co. KGaA, Weinheim, Germany.

[17] "Magnetic Property Measurement System (MPMS®)" [Online]. Available: http://www.qdusa.com/products/mpms.html.

[18] Miller M. K., 2000, Atom Probe Tomography: Analysis at the Atomic Level, Kluwer Academic/Plenum Publishers, New York.

[19] "Groupe de Physique des Matériaux - Principe de fonctionnement de la sonde atomique" [Online]. Available: http://gpm.labos.univ-rouen.fr/spip.php?article170&lang=fr. [Accessed: 03-Oct-2013].

[20] Skomski R., and Sellmyer D. J., 2006, "Intrinsic and Extrinsic Properties of Advanced Magnetic Materials," Handbook of Advanced Magnetic Materials, pp. 1–57.

[21] Belošević-Čavor J., Congiu F., Koteski V., Cekić B., and Concas G., 2006, "Magnetism of the Compounds in the Hf-Co Phase System," Materials Science Forum, **518**, pp. 319–324.